

Geometric integration on spheres and some interesting applications

D. Lewis ^{*} and N. Nigam ^{†*}

April 2, 2002

Abstract

Geometric integration theory can be employed when numerically solving ODEs or PDEs with constraints. In this paper, we present several one-step algorithms of various orders for ODEs on a collection of spheres. To demonstrate the versatility of these algorithms, we present representative calculations for reduced free rigid body motion (a conservative ODE) and a discretization of micromagnetics (a dissipative PDE). We emphasize the role of isotropy in geometric integration and link numerical integration schemes to modern differential geometry through the use of partial connection forms; this theoretical framework generalizes moving frames and connections on principal bundles to manifolds with nonfree actions.

1 Introduction

In this article, we describe a set of algorithms on multiple copies of S^2 (with possibly nonlinear interactions), with applications in material science. The physical processes we are interested in are modeled by PDEs of the form

$$\frac{\partial}{\partial t} \boldsymbol{\mu}(\mathbf{x}, t) = \mathbf{A}(\boldsymbol{\mu}(\mathbf{x}, t)) \times \boldsymbol{\mu}(\mathbf{x}, t), \quad \boldsymbol{\mu}(\mathbf{x}, 0) = \boldsymbol{\mu}_0(\mathbf{x}). \quad (1)$$

Here $\boldsymbol{\mu} : \mathcal{B} \rightarrow \mathbb{R}^3$ is the field describing the physical process of interest, with $\mathbf{x} \in \mathcal{B}$ denoting the spatial variable on some closed, compact subset of \mathbb{R}^3 , and $\mathbf{A}(\boldsymbol{\mu})$ is a (typically nonlinear) function of $\boldsymbol{\mu}$. One immediately notices that $\|\boldsymbol{\mu}(\mathbf{x}, \cdot)\|$ is constant for all time; this constraint should be respected by the numerical methods used to study such systems. Classical numerical integrators fail to preserve this norm, and this motivates our use of geometric integration.

The paper is organized as follows: we begin by introducing a problem in micromagnetics. We then describe the Lie group framework suitable for the general problem (1). The new, and fairly geometric, mathematical constructs of partial moving frames and partial connections, which can be used to select generators for use in numerical methods, are introduced in section 3. Readers who are unfamiliar with modern differential geometry, particularly principal bundles, are advised to skip this section at a first reading. In section 4, we present some one-step algorithms of different orders. An arbitrary function appears in these algorithms; different choices of this function yield distinct discrete trajectories. We describe a possible choice that is related both to moving frames ([1, 2, 3]) and, in the case of a geometric version of the forward Euler method, to discretization error minimization. Work is in progress to identify analogous function choices for higher order methods ([4]). We present the results of numerical experiments carried out using some of these functions for the symplectically reduced free rigid body, a Hamiltonian system on the two-sphere. The conservative nature of the rigid body system facilitates both the derivation of appropriate functions and the assessment of the relative performance of the algorithms. Finally, we present some representative numerical results for micromagnetics that indicate that these geometric integration schemes are competitive with conventional numerical algorithms. Our numerical experiments were carried out using first, second, and fourth order methods.

^{**} Department of Mathematics, University of California, Santa Cruz, [†]Department of Mathematics and Statistics, McGill University, Montreal

1.1 Why use geometric integrators?

One of the intrinsic features of the system (1) is that the vector field $\boldsymbol{\mu}(\mathbf{x}, \cdot)$ evolves on a sphere. However, a classical integrator will update $\boldsymbol{\mu}(\mathbf{x}, t)$ at time t using the approximation

$$\boldsymbol{\mu}(\mathbf{x}, t + \Delta t) \approx \boldsymbol{\mu}(\mathbf{x}, t) + \mathbf{F}(\boldsymbol{\mu}(\mathbf{x}, t), t, \Delta t).$$

The particular form of $\mathbf{F}(\cdot, \cdot, \cdot)$ depends on the algorithm chosen; however, it is clear that such updates correspond to *translations* of $\boldsymbol{\mu}(\mathbf{x}, t)$, not *rotations*. Thus, a classical integrator does not account for the fact that $\boldsymbol{\mu}$ evolves on a sphere. This constraint is difficult to efficiently impose in practice.

A naive approach is to keep track of changes in the norm $\|\boldsymbol{\mu}(\mathbf{x}, t)\|$ during a numerical experiment, and renormalize the iterates after a prescribed tolerance has been exceeded. However, this renormalization is equivalent to the aphysical addition (or subtraction) of energy to the system and is therefore an undesirable solution. In addition, this renormalization would also affect $\mathbf{A}(\boldsymbol{\mu})$. We shall see that in the context of micromagnetics, this change is nontrivial and nonlinear.

Another observation is that the component of $\mathbf{A}(\boldsymbol{\mu})$ parallel to $\boldsymbol{\mu}$ does not influence the solution curve $\boldsymbol{\mu}(\mathbf{x}, t)$. However, this component does alter the discrete trajectories generated by numerical algorithms. An appropriate selection of the normal component can improve the performance of the scheme. Preliminary numerical investigations suggest that such corrections may allow increased accuracy in the capture of key features, e.g. orbits and/or conserved quantities, at a moderate computational cost, without the introduction of significant numerical artifacts, e.g. numerical accelerations.

1.2 Who needs geometric integrators?

The philosophy that numerical algorithms should respect properties intrinsic to the system — momentum conservation, evolution on a manifold, Hamiltonian structure — is not a novel idea. (See, e.g., [5], [6], [7]). Many classes of algorithms have been developed with this guiding principle, especially for energy-conserving or symplectic systems. As far as we know, the application of such methods in the context of numerical micromagnetics is relatively new. Encouraged by the success of these algorithms in an industrial context ([8]), we believe that these techniques will find wider use in the material science community.

Modern magnetic materials are used in an increasingly large number of applications, including thin film read heads and recording media [9], nanocrystalline permanent magnets, and magnetohydrodynamic fluids. In addition, there has been much interest in the use of “smart materials”, including magnetostrictive actuators and organic ferromagnets [10]. These magnetic materials exhibit different responses corresponding to varying magnetic fields. For example, the resistance of a read-head ferromagnetic sensor changes as the device rotates over a recording medium. The magnetization of the material directly interacts with the other physical and chemical characteristics of the material; micromagnetics theory describes this interaction at a microscopic level. Of particularly great interest is the correlation of physical microstructure and magnetization; the ability to predict the response of one to variations in the other is crucial to the further development of these materials and devices.

Another physical system whose mathematical model strongly resembles that of micromagnetics arises in the study of liquid crystals. Nematic and smectic liquid crystals form the basis of the operation of many every-day devices, such as LCD’s, telecommunication devices, thermometers, projection systems — even mood rings. The devices operate on the principle that a suitable applied field will change the orientation of the liquid crystals, while conserving the pointwise-norm. Therefore, the resulting mathematical model has the same constraints as those in the micromagnetics situation. This system has been studied extensively, yet a norm-conserving algorithm has only been presented for an extremely simple situation ([11]).

The study of long-chain molecules such as those occurring in bio-molecular systems yield another possible application area for the methods we develop. These chemical systems have more complicated constraints on the geometry of possible configurations; the configuration sought is one that minimizes a free-energy functional. Statistical thermodynamics considerations permit the reformulation of these optimization problems as evolutions in time on given manifolds to a steady state ([12],[13]). Such studies are used in the development of new drugs.

1.3 A mathematical model of micromagnetics

At any point in time, the magnetization $\boldsymbol{\mu}$ is constant in small regions in the material (termed a domain), and the switching of these domains from one state to another is the basis of the functioning of devices built with these magnetic substances [14]. Ideally the entire device would be one large domain, which would switch instantaneously when an applied field was imposed. In practice, there are several domains, and the net magnetization in a desired direction is not optimal. We are interested in tracking the evolution of these domains, which entails following the local behavior of $\boldsymbol{\mu}$. In industrial applications, a ferromagnetic device is subjected to changing magnetic fields (corresponding to the various applications — a disk moving underneath a read-head, changes in applied voltages for magnetorheological fluids, etc). One is interested in the response of the device to the gradual changing of these external fields.

A model that is widely used in the industry is the *Landau-Lifshitz-Gilbert (LLG)* model of micromagnetics, which describes the evolution of the state of magnetization $\boldsymbol{\mu}$ in a ferromagnetic sensor, occupying a region \mathcal{B} in space. The LLG equation for the magnetization $\boldsymbol{\mu}(x, t)$ is given by

$$\frac{\partial}{\partial t} \boldsymbol{\mu} = -\boldsymbol{\mu} \times \mathbf{H}_{\text{eff}}(\boldsymbol{\mu}) - \lambda \boldsymbol{\mu} \times (\boldsymbol{\mu} \times \mathbf{H}_{\text{eff}}(\boldsymbol{\mu})), \quad \|\boldsymbol{\mu}(\mathbf{x})\| = 1 \quad \forall \mathbf{x} \in \mathcal{B}. \quad (2)$$

Here λ is a damping parameter and \mathbf{H}_{eff} is an effective magnetic field, described in detail below. The first term on the right hand side of (2) describes the (undamped) *Larmor precession* of $\boldsymbol{\mu}$ about \mathbf{H}_{eff} and is derived from first principles [15, 16]. It is observed in physical experiments, however, that changes in magnetization decay in finite time. The second term in (2) is a phenomenological term (called the *Gilbert damping term*, see [17, 18]), added to describe this damping behavior; it cannot be derived from first principles. There are situations under which this system is stiff (see, for example, [19, 20]), and issues of numerical stability of the integration scheme are therefore important. We also thank one of the referees for pointing out [21], where it is suggested that poor representations of the exchange energy may lead to the observed stiff behavior.

The effective field, which causes the magnetization to change, is derived from energy considerations [15] and varies nonlinearly with $\boldsymbol{\mu}$. More precisely,

$$\mathbf{H}_{\text{eff}}(\boldsymbol{\mu}) = A\Delta\boldsymbol{\mu} + \boldsymbol{\mu}_0(-\nabla\phi + \mathbf{H}_{\text{app}}) + K(\boldsymbol{\mu} \cdot \mathbf{e})\mathbf{e}. \quad (3)$$

The parameters A and K are material constants of the permalloy being studied, and $\boldsymbol{\mu}_0$ is the permeability of free-space. The field $A\Delta\boldsymbol{\mu}$ is called the *exchange* field, preventing rapid spatial variations of $\boldsymbol{\mu}$ and the formation of arbitrarily fine domains (see [22, 23] for examples on how this term is computed in general). The final contribution in (3) is due to the nature of ferromagnetic crystals, which causes the magnetic moments to align in preferred directions. This effect is incorporated in the LLG model through the *uniaxial anisotropy* field $K(\boldsymbol{\mu} \cdot \mathbf{e})\mathbf{e}$. The external *applied field* is denoted by \mathbf{H}_{app} . The nonlinear, nonlocal contributions of $\boldsymbol{\mu}$ arise through the *demagnetizing field*, $-\nabla\phi$, where ϕ solves the Poisson problem with suitable boundary

$$\Delta\phi = \nabla \cdot \boldsymbol{\mu} \quad \text{in } \mathbb{R}^3; \quad [\phi] = 0, \quad \left[\frac{\partial\phi}{\partial n} \right] = \boldsymbol{\mu} \cdot \mathbf{n} \quad \text{on } \partial\mathcal{B}, \quad (4)$$

and radiation conditions

$$\phi = o\left(\frac{1}{|\mathbf{x}|}\right) \quad \text{as } |\mathbf{x}| \rightarrow \infty.$$

Here $[u]$ denotes the jump of the function u across $\partial\mathcal{B}$. Many different methods exist for the calculation of this field, including the use of the full Maxwell system, FFT techniques, finite element methods, multigrid approaches, finite differences, and recently, fast multipole methods, [24, 25, 26, 27, 28, 29, 30, 31, 32, 33, 34, 35], among others. While there are still several unsettled issues in the area of demagnetizing field calculations (see [30] for a sharp critique on existing methods), it is not our intention in this project to duplicate this work. Instead, we shall focus on developing a time-stepping method that is robust, accurate, and requires relatively few field evaluations.

Theoretical developments in micromagnetics are driven by industrial demands, and the need for accurate algorithms is now imperative. Conventional algorithms are still being employed for highly sensitive calculations on large sensors, and are becoming increasingly inadequate. Moreover, the time-scales inherent in

these problems vary from nano-seconds (in disk drives) to tens of seconds; hence integration techniques that remain effective over long times are required. An ideal integrator would resolve solutions accurately over very small time steps, while allowing large time steps to be taken when the system evolves over a long period.

1.4 Potential problems with renormalising

We have already described some of the issues with classical integrators with respect to norm conservation. Here we show that renormalizing $\boldsymbol{\mu}$ to conserve the norm while using conventional integrators changes the potential ϕ in a nonlinear fashion; it is easy to construct a simple example in which the renormalization introduces a significant change in the demagnetizing field. Assume that the magnetization $\boldsymbol{\mu}$ satisfies

$$\boldsymbol{\mu}(x, y, z) = a \mathbf{i} + b(x) \mathbf{j}, \quad (5)$$

for some constant a and scalar function b ; here \mathbf{i}, \mathbf{j} denote the usual unit vectors in the x and y directions. Before renormalization, the field \mathbf{M} is divergence-free: $\nabla \cdot \boldsymbol{\mu} \equiv 0$. However, the renormalized field is *not* divergence-free:

$$\nabla \cdot \left(\frac{\boldsymbol{\mu}}{\|\boldsymbol{\mu}\|} \right) = -\frac{a b b'}{(a^2 + b^2)^{3/2}}.$$

The potentials obtained by solving (4) are clearly not the same for the original and renormalized fields. The effect of renormalization on the demagnetization field is particularly significant near domain boundaries. For example, if the function b appearing in (5) is a step function, then the divergence of the renormalized magnetic field is a delta function. We thank F. Reitich, [36], for this illustration of the dangers of normalizing vector fields.

2 Lie group methods for the system $\dot{\boldsymbol{\mu}} = \mathbf{A}(\boldsymbol{\mu}) \times \boldsymbol{\mu}$

We recall that the general system under consideration is

$$\frac{\partial}{\partial t} \boldsymbol{\mu}(\mathbf{x}, t) = \mathbf{A}(\boldsymbol{\mu}(\mathbf{x}, t)) \times \boldsymbol{\mu}(\mathbf{x}, t), \quad \boldsymbol{\mu}(\mathbf{x}, 0) = \boldsymbol{\mu}_0(\mathbf{x}), \quad \mathbf{x} \in \mathcal{B}. \quad (6)$$

The initial condition $\boldsymbol{\mu}_0$ satisfies $\|\boldsymbol{\mu}_0(\mathbf{x})\| = 1$ for all $\mathbf{x} \in \mathcal{B}$, i.e. $\boldsymbol{\mu}_0 : \mathcal{B} \rightarrow S^2$, the unit sphere in \mathbb{R}^3 . Since $\frac{\partial}{\partial t} \|\boldsymbol{\mu}(\mathbf{x}, t)\| = 0$ for all \mathbf{x} and t , $\boldsymbol{\mu}(\cdot, t) : \mathcal{B} \rightarrow S^2$ for all t , the rotation group $SO(3)$ acts transitively on S^2 , i.e. any point on the sphere can be rotated onto any other point on the sphere; hence there are time dependent curves $\tilde{Q} : \mathcal{B} \rightarrow SO(3)$ satisfying

$$\boldsymbol{\mu}(\mathbf{x}, t) = \tilde{Q}(\mathbf{x}, t) \boldsymbol{\mu}_0(\mathbf{x}), \quad \forall \mathbf{x} \in \mathcal{B}. \quad (7)$$

We emphasize that these curves are not uniquely determined by (7).

In the spatially discretized version of the system, we choose N grid points $\mathbf{x}_n, n = 1, 2, \dots, N$ in \mathcal{B} and consider only the values of the magnetic field at those grid points. Given a curve $\boldsymbol{\mu}(\cdot, t) : \mathcal{B} \rightarrow S^2$, we define

$$\mathbf{M}(t) := (\boldsymbol{\mu}(\mathbf{x}_i, t))_{i=1}^N \in \mathcal{M} := (S^2)^N.$$

Where there is no confusion, we suppress the argument t . The fully discretized version of the system (6) is

$$\dot{\mathbf{M}} = \mathbf{A}(\mathbf{M}) \times \mathbf{M}. \quad (8)$$

Here and throughout the paper, vector operations such as cross or inner products on $(S^2)^N$ or $(\mathbb{R}^3)^N$ should be understood as the usual operations in \mathbb{R}^3 performed on each of the N component vectors. The Lie group $\mathcal{G} = (SO(3))^N$ acts transitively, but not freely, on \mathcal{M} . That is, any point in \mathcal{M} can be mapped onto any other point in \mathcal{M} by the action (by component-wise rotations) of \mathcal{G} on \mathcal{M} , but the group element accomplishing any such transformation is not unique. The isotropy subgroup of a point \mathbf{M} in \mathcal{M} (where \mathcal{M} is the group of

transformations fixing \mathbf{M}) is an N -dimensional torus. As in (7), there are smooth time-dependent curves Q in the group \mathcal{G} satisfying

$$\mathbf{M}(t) = Q(t)\mathbf{M}(0), \quad \text{and hence} \quad \dot{\mathbf{M}}(t) = \dot{Q}(t)\mathbf{M}(0). \quad (9)$$

We can use the Lie algebra

$$\mathfrak{G} = (so(3))^N = \{\text{skew symmetric } 3 \times 3 \text{ matrices}\}^N \approx (\mathbb{R}^3)^N$$

of \mathcal{G} , which is the tangent space to \mathcal{G} at the identity, to put (9) into a more familiar and convenient form. The identification of $so(3)$ with \mathbb{R}^3 is implemented using the map $\text{skew} : \mathbb{R}^3 \rightarrow so(3)$ given by

$$\text{skew}[\boldsymbol{\xi}] := \begin{pmatrix} 0 & -\xi_3 & \xi_2 \\ \xi_3 & 0 & -\xi_1 \\ -\xi_2 & \xi_1 & 0 \end{pmatrix},$$

i.e. $\text{skew}[\boldsymbol{\xi}]\mathbf{x} = \boldsymbol{\xi} \times \mathbf{x}$ for all $\mathbf{x} \in \mathbb{R}^3$. The matrix commutator bracket on $so(3)$ corresponds to the cross product on \mathbb{R}^3 under this identification.

Given any differentiable curve $Q(t)$ in \mathcal{G} , there exists a curve $\boldsymbol{\xi}(t) \in (\mathbb{R}^3)^N$ satisfying

$$\dot{Q}(t) = \text{skew}[\boldsymbol{\xi}(t)]Q(t),$$

where the product of $\text{skew}[\boldsymbol{\xi}]$ and Q is the usual matrix product. Thus the system (8) is equivalent to

$$\dot{\mathbf{M}}(t) = \dot{Q}(t)\mathbf{M}_0 = \text{skew}[\boldsymbol{\xi}(t)]Q(t)\mathbf{M}_0 = \boldsymbol{\xi}(t) \times \mathbf{M}(t). \quad (10)$$

Comparing (10) to (8), we see that

$$\boldsymbol{\xi}(t) = \boldsymbol{\omega}(\mathbf{M}(t)), \quad \text{where} \quad \boldsymbol{\omega}(\mathbf{M}) = \mathbf{A}(\mathbf{M}) + \sigma(\mathbf{M})\mathbf{M} \quad (11)$$

for an arbitrary scalar function $\sigma : \mathcal{M} \rightarrow \mathbb{R}$. The flexibility in the choice of map σ arises from the non-freeness of the action of $SO(3)$ on S^2 , and thus the action of \mathcal{G} on \mathcal{M} ; distinct ODEs

$$\dot{Q} = \text{skew}[\boldsymbol{\omega}(Qm)]Q \quad \text{and} \quad \dot{Q} = \text{skew}[\tilde{\boldsymbol{\omega}}(Qm)]Q,$$

where $\boldsymbol{\omega}(m) - \tilde{\boldsymbol{\omega}}(m) \in \text{span}[m]$ for all $m \in S^2$, will typically have distinct solution curves in $SO(3)$, but the images in S^2 of those solution curves under the map $Q \mapsto Q \cdot m_0$ will coincide.

When numerically simulating (8), we want a time-stepping method that ensures that $\mathbf{M}_n \in \mathcal{M}$, i.e. that the norms of the component vectors are identically equal to one. We can regard (10) and (11) as defining a family of ODEs

$$\dot{Q} = \text{skew}[\boldsymbol{\omega}(Q\mathbf{M}_0)]Q,$$

parametrized by $\mathbf{M}_0 \in \mathcal{M}$ and $\sigma : \mathcal{M} \rightarrow \mathbb{R}$, on the group \mathcal{G} and use the techniques developed for geometric integration on Lie groups to determine approximate discrete solution curves of these ODE (see [37, 38, 39, 40] and the references therein). When combined with the action of \mathcal{G} on \mathcal{M} , these techniques yield geometric integration schemes for (6) that exactly preserve the constraint $\mathbf{M}_n \in \mathcal{M}$, regardless of the step size or the order of the integrator.

The key idea is the following. Suppose we are given a (right) trivialized form $\dot{g} = \xi(g)g$ of an ODE on a Lie group G and an *algorithmic exponential* $\text{Exp} : \mathfrak{g} \rightarrow G$ mapping the Lie algebra \mathfrak{g} of G into G . Then an integrator of order k corresponds to an update of the form

$$g_{n+1} = \text{Exp}(F(g_{n-p}, \dots, g_n, \Delta t))g_n,$$

for some map $F : G^{p+1} \times \mathbb{R} \rightarrow \mathfrak{g}$ determined by the algorithm and the generator ξ . Here we consider only one step methods, with $p = 0$. We emphasize that the algorithmic exponential need not be the true exponential of the Lie group, or even a good approximation to the true exponential; all that we require is that it map

algebra elements exactly into the group G and that the algorithmic exponential of the zero vector in \mathfrak{g} equal the identity element of G . For example, the Cayley transform, given by

$$\text{cay}(\boldsymbol{\xi}) = (I + \text{skew}[\boldsymbol{\xi}/2])(I - \text{skew}[\boldsymbol{\xi}/2])^{-1},$$

is an algorithmic exponential for the rotation group that has long been used in computational mechanics. The Cayley transform has long been used to implement exact rotations in elasticity and plasticity simulations; see, for example, [41, 42]). More recently, it has been utilized in the geometric integration of a wide variety of mechanical systems, including the LLG equations; see [37, 38, 43, 44, 45], and references therein. Algorithms of arbitrarily high order can be constructed using the Cayley transform, despite the fact that is only a second order approximation of the matrix exponential of $SO(3)$. (Note that the Cayley transform is, in fact, an algorithmic exponential for any matrix group determined by a quadratic constraint. See, e.g. [46].) For the rotation group $SO(3)$ on \mathbb{R}^3 , both the true matrix exponential and the Cayley transform can be efficiently evaluated and have frequently been used as algorithmic exponentials. The true exponential takes the form

$$\exp(\boldsymbol{\xi}) = I + \frac{\sin \|\boldsymbol{\xi}\|}{\|\boldsymbol{\xi}\|} \text{skew}[\boldsymbol{\xi}] + \frac{1 - \cos \|\boldsymbol{\xi}\|}{\|\boldsymbol{\xi}\|^2} \text{skew}[\boldsymbol{\xi}]^2.$$

The image of a vector $\mathbf{x} \in \mathbb{R}^3$ under the action of $\text{cay}(\boldsymbol{\xi})$ takes the simple, readily evaluated form

$$\text{cay}(\boldsymbol{\xi})\mathbf{x} = \mathbf{x} + \frac{1}{1 + \|\boldsymbol{\xi}/2\|^2} \left[\boldsymbol{\xi} \times \mathbf{x} + \frac{1}{2} \boldsymbol{\xi} \times (\boldsymbol{\xi} \times \mathbf{x}) \right].$$

Hence we shall use the Cayley transform (actually, N copies of the Cayley transform) as our algorithmic exponential $\text{Exp} : \mathfrak{G} \rightarrow \mathcal{G}$. We observe that the Cayley transform has the advantage that the entries of $\text{cay}(\boldsymbol{\xi})$ are rational functions of the components of $\boldsymbol{\xi}$; in particular, no trigonometric functions need be evaluated.

To summarize this section, we have rewritten the discrete system

$$\dot{\mathbf{M}}(t) = \mathbf{A}(\mathbf{M}) \times \mathbf{M}(t), \quad \mathbf{M}(0) = \mathbf{M}_0$$

as an ODE

$$\dot{Q}(t) = \text{skew}[\boldsymbol{\omega}(Q(t)\mathbf{M}_0)]Q(t).$$

on the Lie group $\mathcal{G} = (SO(3))^N$. We now need to describe choices of infinitesimal update maps F and generators \mathbf{A} that determine one step numerical updates $Q_{n+1} = \text{Exp}(\mathbf{F}(Q_n\mathbf{M}_0, \Delta t))Q_n$ and associated updates

$$\mathbf{M}_{n+1} = Q_{n+1}\mathbf{M}_0 = \text{Exp}(\mathbf{F}(\mathbf{M}_n, \Delta t))\mathbf{M}_n$$

with specified properties, e.g. a specified order of overall accuracy. The construction of suitable updates is the subject of the next section.

3 Generator selection — Expansions, curvature, and partial connections

A natural and obvious goal in selection of a numerical scheme is the achievement of the highest possible accuracy working within the given constraints. However, the prioritization of the constraints (efficiency, stability, developer effort, preservation of key features of the modeled system, etc.) can lead to significantly different approaches to the achievement of this goal and correspondingly different schemes. For the purposes of this discussion, we shall assume that we are given a family of one step methods of the form

$$(\mathbf{M}_{n+1})_j = \text{cay}(\mathbf{F}(\mathbf{M}_n, \Delta t)_j)(\mathbf{M}_n)_j \quad j = 1, \dots, N \quad (12)$$

for some map $\mathbf{F} : \mathcal{M} \times \mathbb{R} \rightarrow (\mathbb{R}^3)^N$. (Recall that $\mathcal{M} := (S^2)^N$.)

We can optimize accuracy within this family of methods by selecting an appropriate isotropy algebra correction; specifically, we shall first compute the update generator given some ‘default’ choice of generator, and then use that generator to determine an element of the isotropy algebra of the current state that minimizes the discretization error for that update. We will derive conditions specifying this choice of isotropy element for algorithms on \mathcal{M} utilizing the action of \mathcal{G} using a traditional series expansion approach to the computation of the discretization error. (See [3] for the application of this approach and those discussed below to general homogeneous manifolds.) Subsequently, we will discuss some more geometric and, in some cases, less computationally intensive, approaches to this task.

The geometric approach most closely related to the naive series expansion treatment is the use of geodesic curvature to characterize the essential information about curves on manifolds, e.g.; solution curves of differential equations. A less directly related approach, but one that coincides with the direct error minimization approach for the forward Euler method on \mathcal{M} is the use of a partial moving frame and the associated partial connection form to determine a choice of generator. We shall define these constructions in section 3.2.

3.1 Algorithms on S^2

To demonstrate the influence of the isotropy algebra on discrete trajectories, we first study the action of the rotation group $SO(3)$ on a single sphere S^2 . The techniques we use in analysing the case of a single sphere immediately generalize to \mathcal{M} . An autonomous vector field X on S^2 satisfies $\langle X(m), m \rangle = 0$ for all $m \in S^2$; hence there exists a (nonunique) map $A : S^2 \rightarrow \mathbb{R}^3$, called a *generator* of X , satisfying

$$X(m) = A(m) \times m$$

on S^2 . Recall from our earlier discussion that distinct choices of generator A typically yield distinct discrete trajectories when used in a numerical algorithm of the form (12). We will compare the performance of various schemes with two different choices of generator. The first choice is the ‘default’ or ‘natural’ one, which is not assumed to have any particular geometric properties. For the rigid body system, we will take the body angular velocity as our default generator. For arbitrary vector fields X , there need not be a natural choice of generator; our intent here is to make a plausible choice of generator that one might make if the issue of isotropy were not taken into account. The second choice is the orthogonal generator, i.e. the unique map $A_o : S^2 \rightarrow \mathbb{R}^3$ satisfying

$$X(m) = A_o(m) \times m \quad \text{and} \quad \langle A_o(m), m \rangle = 0$$

for all $m \in S^2$.

A general and direct, but potentially computationally intensive, approach to the choice of a generator that reduces the discretization error is to compute the lowest order nonzero term in the series expansion for the discretization error for the family of algorithms under consideration, leaving the isotropy algebra component of the generator as an undetermined parameter, and thus determine conditions on the isotropy component that minimize the error. See [3] for a general treatment of this approach and section 4.1 for the derivation of the optimal generator choice for our forward Euler algorithm for the LLG system. Here we briefly explore some alternatives to this approach that have natural geometric interpretations.

We consider an Euler update of the form

$$\tilde{\mathcal{F}}_{\Delta t}(m) = \text{Exp}(\Delta t (A_o(m) + \sigma(m) m)), \tag{13}$$

where σ determines the isotropy (normal component) contribution. In the special case that the algorithmic exponential is given by a rescaling of the usual matrix exponential, e.g. by the Cayley transform, (13) satisfies

$$\tilde{\mathcal{F}}_{\Delta t}(m) = \exp(\tau(m, \Delta t) (A_o(m) + \sigma(m) m))$$

for some rescaling τ of time. Hence, in this case, $\tilde{\mathcal{F}}_t(m)$ is given by a rigid rotation of m about an axis depending only on m . Hence the curve

$$\Gamma_\epsilon(m) = \left\{ \tilde{\mathcal{F}}_t(m) : |t| \leq \epsilon \right\}$$

is a segment of a circle in S^2 . Our goal is to choose σ so as to obtain the best circular approximation at m to the true orbit segment

$$\mathcal{O}_\epsilon(m) = \{\mathcal{F}_t(m) : |t| \leq \epsilon\}.$$

If $X(m) \neq 0$, then the optimal circular approximation to $\mathcal{O}_\epsilon(m)$ at m can be characterized using the geodesic curvature

$$k_g(m) = \frac{\langle (X \cdot \nabla)X(m), m \times X(m) \rangle}{\|X(m)\|^3}$$

of $\mathcal{O}_\epsilon(m)$ at m . The best circular approximation to $\mathcal{O}_\epsilon(m)$ at m is tangent to $X(m)$ at m and has geodesic curvature equal to that of $\mathcal{O}_\epsilon(m)$ at m . The first condition is clearly satisfied for any consistent update. The geodesic curvature $\tilde{k}_g(m)$ of $\Gamma_\epsilon(m)$ is easily seen to satisfy $|\tilde{k}_g(m)| = |\cot \phi|$, where ϕ is the angle between m and $A_o(m) + \sigma(m)m$ (see, e.g. [47], p. 249); thus $|\tilde{k}_g(m)| = |\sigma(m)|/\|A_o(m)\|$. Hence optimal orbit capture within the class of updates (13) is obtained using

$$\sigma_{\text{cor}}(m) := k_g(m)\|X(m)\|. \quad (14)$$

If $\mathcal{O}_\epsilon(m)$ is itself a segment of a circle, then σ_{cor} yields $\Gamma_\epsilon(m) = \mathcal{O}_\epsilon(m)$. Hence any torsion-free orbits, e.g. the separatrices of the reduced rigid body equations, are captured exactly by this version of the Euler method. Note that the choice A_o is suboptimal for the Euler method unless $k_g \equiv 0$ along the tractory of interest, i.e. unless the desired trajectory is a great circle.

For higher order methods, the axis of rotation used in the update map $\tilde{\mathcal{F}}_t$ is typically time dependent and hence the corresponding algorithmic trajectory segment typically is not circular (i.e. it has nonzero torsion). Hence the simple argument used in the preceding paragraph cannot be applied. However, the strategy of curvature-matching can still be followed. Since a smooth curve on a two dimensional manifold in \mathbb{R}^3 is determined up to a time reparametrization by its geodesic curvature, we can determine the conditions on the generator imposed by the restriction that the geodesic curvature of $\tilde{\mathcal{F}}_t(m)$ match that of $\mathcal{F}_t(m)$ to some order. The higher order derivatives of the curvature can either be determined analytically for a given vector field X or numerically approximated using standard difference schemes.

More generally, the choice a generator of a vector field on a homogeneous manifold can be viewed as a special case of the choice of a partial connection form, which generalizes to nonfree actions the classical connection form on a principal bundle. A partial connection form is a Lie algebra-valued one-form with appropriate equivariance properties. In section 3.2 we state the relevant definitions and present a family of partial connection forms on open subsets of S^2 that yield a discretization error-minimizing algorithm and determine an algorithm that captures orbits to second order for any dynamical system on a single copy of S^2 . The interested reader is referred to [4] for a more detailed treatment of partial connection forms and related constructions.

3.2 Partial connection forms

We now briefly discuss a general geometric approach to the selection of generators, using a generalization of the connection form on a principal bundle. For a more detailed treatment of this generalization and proofs of the assertions given below, see Lewis et al. [2002]. Let \mathcal{P} be a principle bundle, that is, a manifold \mathcal{P} acted on by a Lie group G . Let the action of $g \in G$ in \mathcal{P} be denoted by $g \cdot p = \Phi_g(p) = \hat{\Phi}_p(g)$, $\forall g \in G, p \in \mathcal{P}$. Let $\mathfrak{g} := T_e G$ denote the algebra of G and let $\mathfrak{g} \cdot p := \left\{ T_e \hat{\Phi}_p \cdot \xi : \xi \in \mathfrak{g} \right\}$. Recall that a *connection* on a principal bundle \mathcal{P} is a distribution Γ satisfying

$$T_p \mathcal{P} = \mathfrak{g} \cdot p \oplus \Gamma_p \quad \text{and} \quad T_p \Phi_g \cdot \Gamma_p = \Gamma_{g \cdot p},$$

for all $p \in \mathcal{P}$ and $g \in G$. Specification of a connection Γ is equivalent to specification of an equivariant \mathfrak{g} -valued one-form α , called the *connection form*, satisfying

$$\alpha \circ T_e \hat{\Phi}_p = \text{id}, \quad \text{i.e.} \quad \alpha(p)(\xi_{\mathcal{P}}(p)) = \xi \quad \text{for all } \xi \in \mathfrak{g},$$

for all $p \in \mathcal{P}$. By equivariance we mean that $\alpha \circ T\Phi_g = \text{Ad}_g \circ \alpha$ for all $g \in G$. The connection Γ and connection form α are related by the condition $\ker[\alpha(p)] = \Gamma_p$ for all $p \in \mathcal{P}$. (See, e.g., [48] for a detailed presentation of the properties of connections and connection forms.)

The equivariance properties of connections and connection forms typically cannot be preserved in the context of nonfree actions, hence we relax these conditions, requiring only equivariance with respect to specified representatives of the isotropy equivalence classes. A map $\beta : G \times \mathcal{M} \rightarrow G$ is a *slip map* if $\beta(g, m) \cdot m = g \cdot m$ for all $g \in G$ and $m \in \mathcal{M}$. A (singular) distribution \aleph assigning a complement \aleph_m to $\mathfrak{g} \cdot m$ in $T_m\mathcal{M}$ to each point $m \in \mathcal{M}$ is a *partial connection* if there is a slip map β satisfying

$$T_m\Phi_{\beta(g,m)} \cdot \aleph_m = \aleph_{g \cdot m}$$

for all $g \in G$ and $m \in \mathcal{M}$. A *partial connection form* with slip map β is a \mathfrak{g} -valued one-form α on \mathcal{M} satisfying

$$\alpha(m)(\eta_{\mathcal{M}}(m)) = \eta \pmod{\mathfrak{g}_m}, \quad \text{i.e.} \quad T_e\hat{\Phi}_m(\alpha \circ T_e\hat{\Phi}_m - \text{id}) = 0$$

and

$$\Phi_{\beta(g,m)}^* \alpha(m) = \text{Ad}_{\beta(g,m)} \alpha(m) \pmod{\mathfrak{g}_{g \cdot m}}$$

for all $g \in G$ and $m \in \mathcal{M}$.

One natural source of partial connections is a generalization of a *moving frame*, in the modern sense introduced by Fels and Olver ([49], [50]), i.e. a smooth equivariant map $\rho : \mathcal{P} \rightarrow G$ on a manifold \mathcal{P} with a free group action. Recall that a principal bundle \mathcal{P} is trivial if there exists a global section, i.e. a smooth map $\Sigma : \mathcal{M} \rightarrow \mathcal{P}$ from the base manifold \mathcal{M} into \mathcal{P} such that each group orbit $G \cdot p$ in \mathcal{P} intersects $\Sigma(\mathcal{M})$ exactly once and the projection $\pi : \mathcal{P} \rightarrow \mathcal{M}$ satisfies $\pi \circ \Sigma = \text{id}$. This condition corresponds to the existence of a moving frame. Specifically, a global section Σ and associated moving frame ρ are related by the equality

$$\Sigma(\pi(p)) = \rho(p)^{-1} \cdot p$$

for all $p \in \mathcal{P}$. A global section determines a flat connection, namely the connection that assigns to any point $\Sigma(m)$ the subspace $T_m\Sigma \cdot T_m\mathcal{M}$. If we introduce the notation $\tilde{D}\gamma : T\mathcal{P} \rightarrow \mathfrak{g}$ to denote the right trivialization of the linearization of a map $\gamma : \mathcal{P} \rightarrow G$, i.e.

$$\tilde{D}\gamma(\delta p) := T_p(R_{\gamma(p)^{-1}} \circ \gamma) \delta p$$

for any $p \in \mathcal{P}$ and $\delta p \in T_p\mathcal{P}$, then $\tilde{D}\rho$ is the connection form of the connection determined by Σ .

The rotation group $SO(3)$ acts transitively on S^2 and freely and transitively on the unit tangent bundle $U(S^2) = \{u \in TS^2 : \|u\| = 1\}$. The map $\rho : U(S^2) \rightarrow SO(3)$ taking $u \in U_m S^2$ to the orthogonal matrix with columns $(m, u, m \times u)$ is a (left) moving frame with associated connection form

$$\tilde{D}\rho(\delta u) = m \times \delta m + \langle u \times \delta u, m \rangle m,$$

where $\delta u \in T_u U(S^2)$, with $m = \pi(u)$ and $\delta m = T_u\pi \delta u$. (Here $\pi : U(S^2) \rightarrow S^2$ denotes the canonical projection.) Note that we will regard u both as a tangent vector to the sphere at m and as a unit vector in \mathbb{R}^3 .

Moving frames can be extended to manifolds with nonfree actions as follows: A (smooth) map $\phi : \mathcal{M} \rightarrow G$ is a (left) *partial moving frame* if

$$\phi_g(m) := \phi(g \cdot m)(\phi(m))^{-1} \tag{15}$$

satisfies

$$\phi_g(m) \cdot m = g \cdot m$$

for all $g \in G$ and $m \in \mathcal{M}$. A *partial moving frame* on a submanifold \mathcal{S} of a manifold \mathcal{M} with a G action is a map $\phi : \mathcal{S} \rightarrow G$ satisfying (15) for any $m \in \mathcal{S}$ and any $g \in G$ such that $g \cdot m \in \mathcal{S}$. The trivialized linearization $\tilde{D}\phi$ of a partial moving frame $\phi : \mathcal{M} \rightarrow G$ is a partial connection form, with associated slip map $\beta(g, m) = \phi_g(m)$. We refer to the trivialized linearization $\tilde{D}\phi$ as the partial connection form associated to the partial moving frame ϕ .

If a group G acts transitively on a manifold \mathcal{M} , then every group orbit is equal to the entire manifold. In this situation, a (partial) connection form α assigns to each tangent vector a generator of that vector, so that

$$(\alpha(m)(\delta m))_{\mathcal{M}(m)} = \delta m$$

for all $\delta m \in T_m\mathcal{M}$ and all $m \in \mathcal{M}$. In particular, given a vector field X on \mathcal{M} , the map $\omega := \iota_X\alpha : \mathcal{M} \rightarrow \mathfrak{g}$, i.e. $\omega(m) = \alpha(m)(X(m))$, satisfies

$$\omega(m)_{\mathcal{M}(m)} = X(m)$$

for all $m \in \mathcal{M}$. Hence (partial) connection forms can be used to construct geometric integration schemes on manifolds with transitive actions. We are currently investigating the role of geometrically motivated choices of partial connection forms in the design of efficient geometric integration algorithms. As can be seen in the example discussed below, simple, natural choices of partial connection forms can lead to significant improvement in numerical performance.

To illustrate the somewhat abstract geometric constructions described above, we now present a moving frame associated to the action of the rotation group $SO(3)$ on the unit tangent bundle $U(S^2)$ of the sphere S^2 and an associated family of partial moving frames on S^2 . The partial connection form (which, in this case, is simply a map from the sphere to \mathbb{R}^3) of one of these partial moving frames yields the discretization error-minimizing generators used in the versions of the forward Euler method described in sections 4.1 and 5. As we shall see, this partial connection form and the associated generators can be derived without the use of the expansion of the discretization error.

Any unit vector field Y on a submanifold \mathcal{M} of S^2 determines a partial moving frame $\phi = \rho \circ Y$ on \mathcal{M} , with partial connection form

$$\tilde{D}\phi(\delta m) = m \times \delta m + \langle Y(m) \times (DY(m) \cdot \delta m), m \rangle m. \quad (16)$$

The map ϕ_g associated to $g \in SO(3)$ is $\phi_g(m) = g \exp(\theta(g, m) m)$, where $\theta(g, m)$ denotes the angle between $g^{-1}Y(gm)$ and $Y(m)$. Given an ODE $\dot{m} = X(m)$, we can set $Y(m) = X(m)/\|X(m)\|$ on some set $\mathcal{M} \subset S^2$ containing no equilibria (i.e. zeroes of X); in this case, (16) takes the form

$$\tilde{D}\phi(m)(\delta m) = m \times \delta m + \frac{\langle (\delta m \cdot \nabla)X, m \times X(m) \rangle}{\|X(m)\|^2} m. \quad (17)$$

In particular,

$$\tilde{D}\phi(m)(X(m)) = m \times X(m) + k_g(m) \|X(m)\| m, \quad (18)$$

where $k_g(m)$ denotes the geodesic curvature of the curve $m(t)$ in S^2 .

The partial connection form (16) can be used to select the isotropy correction map σ used in (13). Following (18), we set

$$\sigma(m)(x) := \begin{cases} k_g(m)(x) \|X(m)(x)\| & X(m)(x) \neq 0 \\ 0 & X(m)(x) = 0 \end{cases}. \quad (19)$$

In our numerical implementation (19), we approximate $k_g(m)$ using the identity

$$k_g(m) = \frac{\langle \ddot{m}, m \times \dot{m} \rangle}{\|\dot{m}\|^3} = -\frac{\langle \dot{\omega}, \omega \times m \rangle}{\|\omega\|^3}$$

for a curve $m(t)$ in S^2 with nonzero velocity $\dot{m} = \omega \times m$, where ω is orthogonal to m , and replacing \dot{m} and \ddot{m} with finite difference approximations.

4 A collection of geometric integrators

Recall that an update of the form

$$Q_{n+1} = \text{Exp}(\mathbf{F}(Q_n \mathbf{M}_0, \Delta t)) Q_n,$$

where $\text{Exp} : \mathfrak{G} \rightarrow \mathcal{G}$ satisfies $(\text{Exp}(\boldsymbol{\xi}))_j = \text{cay}(\boldsymbol{\xi}_j)$, determines a one step method on the Lie group \mathcal{G} , where $\mathbf{F} : \mathcal{G} \times \mathbb{R} \rightarrow \mathfrak{G}$ is determined by the generator and the selected scheme, and Δt denotes the time step. Given an ODE $\dot{\mathbf{M}}(t) = \mathbf{A}(\mathbf{M}) \times \mathbf{M}$ on \mathcal{M} , we will construct updates of the form

$$\mathbf{M}_{n+1} = \text{Exp}(\mathbf{F}(\mathbf{M}_n, \Delta t)) \cdot \mathbf{M}_n, \quad (20)$$

It is our objective to identify several classes of infinitesimal update maps F , leading to algorithms of first, second, and fourth order.

4.1 Discretization error reduction through choice of σ

As was previously discussed, the normal component of the generator \mathbf{A} does not influence the solution curves of the original ODE. Thus, if we have a numerical algorithm of order n , this component does not affect the solution up to order n . However, it typically does appear in the higher order terms of the approximation, and theoretically a suitable choice of this component will reduce the discretization error. For the forward Euler scheme an optimal choice of σ , in the sense that this choice minimizes the discretization error, also has a natural geometric interpretation. Here we derive this map σ using a direct discretization error calculation; in the following section we shall discuss various geometric considerations that can be used in the selection of the generator to be used in a Lie group integration scheme.

We consider consistent algorithms using standard methods on the tangential component of ξ . The normal component is treated as a function of the tangential one; we shall see that a component of the local discretization error at second order can be eliminated by a suitable choice of the normal component of the lowest order term in ξ . For the sake of simplicity, we consider here only the lowest order case, in which the discretization error of a first order method is reduced by an appropriate selection of σ . This is a particular example of a more general result covering a large class of manifolds and higher order algorithms. (See [3, 4].) Work is in progress (Lewis, Nigam, Olver) to possibly extend these or related results to an even larger class of systems, including the full discretized LLG system.

We begin by examining the flow \mathcal{F}_t of the ODE $\dot{\mathbf{M}} = \mathbf{A}(\mathbf{M}) \times \mathbf{M}$ on \mathcal{M} . This flow satisfies

$$\mathcal{F}_{\Delta t}(\mathbf{M}) = \mathbf{M} + \Delta t \mathbf{A} \times \mathbf{M} + \frac{\Delta t^2}{2} \left(\mathbf{A} \times (\mathbf{A} \times \mathbf{M}) + \dot{\mathbf{A}} \times \mathbf{M} \right) + \mathcal{O}(\Delta t^3).$$

If the algorithmic update $\tilde{\mathcal{F}}_{\Delta t} : \mathcal{M} \rightarrow \mathcal{M}$ is given by

$$\tilde{\mathcal{F}}_{\Delta t}(\mathbf{M}) := \text{Exp}(\mathbf{F}(\mathbf{M}, \Delta t)) \cdot \mathbf{M}$$

for some map $\mathbf{F}(\mathbf{M}, \Delta t) := \sum_{j=1}^{\infty} \frac{\Delta t^j}{j!} \boldsymbol{\xi}_j(\mathbf{M})$ and $\text{Exp} : \mathbb{R}^3 \approx \mathfrak{so}(3) \rightarrow \text{SO}(3)$ agrees with the exponential map to second order (e.g. Exp is the Cayley transform), then

$$\begin{aligned} \tilde{\mathcal{F}}_{\Delta t}(\mathbf{M}) &= \left(I + \Delta t \text{skew}[\mathbf{A}] + \frac{1}{2} \Delta t^2 \text{skew}[\mathbf{A}]^2 + \mathcal{O}(\Delta t^3) \right) \mathbf{M} \\ &= \left(I + \Delta t \text{skew}[\boldsymbol{\xi}_1] + \frac{1}{2} \Delta t^2 \left(\text{skew}[\boldsymbol{\xi}_2] + \text{skew}[\boldsymbol{\xi}_1]^2 \right) + \mathcal{O}(\Delta t^3) \right) \mathbf{M} \\ &= \mathbf{M} + \Delta t \boldsymbol{\xi}_1 \times \mathbf{M} + \frac{\Delta t^2}{2} \left(\boldsymbol{\xi}_1 \times (\boldsymbol{\xi}_1 \times \mathbf{M}) + \boldsymbol{\xi}_2 \times \mathbf{M} \right) + \mathcal{O}(\Delta t^3). \end{aligned}$$

We now derive conditions on the terms $\boldsymbol{\xi}_1, \boldsymbol{\xi}_2, \dots$ in the series expansion of F yielding algorithms of increasingly high order. The consistency condition for $\tilde{\mathcal{F}}_{\Delta t}$ is $\mathbb{P}_{\mathbf{M}}(\boldsymbol{\xi}_1 - \mathbf{A}) = 0$, where $\mathbb{P}_{\mathbf{M}}$ denotes component-wise projection onto the orthogonal complements of the component vectors of \mathbf{M} , i.e. $\langle (\mathbb{P}_{\mathbf{M}}\boldsymbol{\xi})_j, \mathbf{M}_j \rangle = 0$, $j = 1, \dots, N$. If $\tilde{\mathcal{F}}_{\Delta t}$ is consistent, then, setting $\sigma_1 := \langle \boldsymbol{\xi}_1, \mathbf{M} \rangle$, the local discretization error is

$$\begin{aligned} \frac{\tilde{\mathcal{F}}_{\Delta t}(\mathbf{M}) - \mathcal{F}_{\Delta t}(\mathbf{M})}{\Delta t} &= \frac{\Delta t}{2} \left(-\sigma_1 \mathbf{M} \times (\boldsymbol{\xi}_1 \times \mathbf{M}) + (\boldsymbol{\xi}_2 - \dot{\mathbf{A}}) \times \mathbf{M} \right) + \mathcal{O}(\Delta t^2) \\ &= \frac{\Delta t}{2} \left(-\sigma_1 \mathbf{A} + (\boldsymbol{\xi}_2 - \dot{\mathbf{A}}) \times \mathbf{M} \right) + \mathcal{O}(\Delta t^2). \end{aligned}$$

The algorithm is thus second-order accurate iff

$$\langle \xi_2 - \dot{\mathbf{A}}, \mathbf{A} \rangle = 0 \quad \text{and} \quad \sigma_1 \langle \mathbf{A}, \mathbf{A} \rangle = \langle (\xi_2 - \dot{\mathbf{A}}) \times \mathbf{M}, \mathbf{A} \rangle. \quad (21)$$

In our geometric version of the forward Euler method with $\mathbf{F}(\mathbf{M}, \Delta t) = \mathbf{A}(\mathbf{M})$, $\xi_j = 0$ for $j > 1$; thus this method will not be second order. However, we are free to choose σ_1 so as to satisfy the second equality in (21), e.g.

$$\sigma(\mathbf{M}, \Delta t) = \frac{\langle \Delta \mathbf{A}(\mathbf{M}, \Delta t), \mathbf{A}(\mathbf{M}) \times \mathbf{M} \rangle}{\|\mathbf{A}(\mathbf{M})\|^2} + \mathcal{O}(\Delta t^2), \quad (22)$$

where $\Delta \mathbf{A}(\mathbf{M}, \Delta t)$ is some first order approximation to $\dot{\mathbf{A}}(\mathbf{M})$ (e.g., a discrete difference approximation), yielding a discretization error-minimizing member of the family of algorithms with $\mathbf{F}(\mathbf{M}, \Delta t) = \mathbf{A}(\mathbf{M}) + \sigma(\mathbf{M}, \Delta t)\mathbf{M}$.

Analogous expansions can be used to minimize the discretization error of higher order methods. However, the symbolic calculation of such expansions for high order schemes is, at present, relatively laborious and does not seem tractable for systems such as the LLG equations, in which the generator \mathbf{A} is determined in part (the demagnetization field) by a nonlinear PDE.

4.2 First order methods

Using (20), we now define geometric one-step methods that are natural analogs of the standard explicit and implicit Euler methods:

$$\mathbf{F}(\mathbf{M}, \Delta t) = \begin{cases} \mathbf{A}(\mathbf{M}) + \sigma(\mathbf{M}, \Delta t)\mathbf{M} & \text{forward Euler,} \\ \tilde{\mathbf{A}}(\mathbf{M}, \Delta t) + \tilde{\sigma}(\mathbf{M}, \Delta t)\mathbf{M} & \text{implicit Euler,} \end{cases} \quad (23)$$

where $\tilde{\mathbf{A}}(\mathbf{M}, \Delta t)$ denotes the solution of the implicit equation $\xi = \mathbf{A}(\text{Exp}(\Delta t \xi)\mathbf{M})$ and the scalar functions σ and $\tilde{\sigma}$ are as yet unspecified.

The numerical results presented in sections 3 and 6 illustrate the effect of the parameter σ on the discrete trajectories determined by the forward Euler algorithm when applied to rigid body dynamics and the LLG micromagnetism model. We shall see that in the rigid body system, σ satisfying (22) yields second order accuracy in energy tracking, and thus second order orbit capture for this conservative system. In the micromagnetics simulations, where damping plays a crucial role in the long term dynamics, large values of σ cause the trajectories to sharply diverge from those of the ordinary forward Euler; however, the final state is the same. A closer look at the LLG equation shows that a larger value of σ corresponds to the inclusion of more precession in the trajectory. These numerical results clearly show that different choices of the parameter σ lead to significantly different numerical trajectories and thus motivate the search for an ‘‘optimal’’ value of σ . In section 3 we describe a general geometric approach to selecting values for σ ; in section 4.1 we show that when used with the forward Euler method, this choice of σ minimizes the discretization error. (See [3] for a description of this approach for more general manifolds.)

4.3 Second order methods

We consider four second order methods modeled on the classic Heun (RK2) algorithm.

In the first, we use the ‘default’ generator \mathbf{A} in the Heun method, i.e.

$$\mathbf{F}_{\text{def}}^{\text{RK2}}(\mathbf{M}, \Delta t) := \frac{1}{2} (\mathbf{A}(\text{cay}(\Delta t \mathbf{A}(\mathbf{M}))\mathbf{M}) + \mathbf{A}(\mathbf{M})).$$

The second method, $\mathbf{F}_{\text{orth}}^{\text{RK2}}$, is entirely analogous, but with \mathbf{A} replaced with the orthogonal generator \mathbf{A}_o , where

$$\mathbf{A}_o(\mathbf{M}) := \mathbf{A}(\mathbf{M}) - (\mathbf{M} \cdot \mathbf{A}(\mathbf{M}))\mathbf{M},$$

and hence $\langle (\mathbf{A}_o(\mathbf{M}))_j, \mathbf{M}_j \rangle = 0$, $j = 1, \dots, N$.

In the third method, the infinitesimal rotation determined by applying the Heun method to the default generator \mathbf{A} is modified by addition of an appropriate isotropy element to yield a higher order of orbit capture; specifically,

$$\mathbf{F}_{\text{dcor}}^{\text{RK2}}(\mathbf{M}, \Delta t) := \mathbf{F}_{\text{def}}^{\text{RK2}}(\mathbf{M}, \Delta t) + \Delta t^2 \sigma_{\text{def}}(\mathbf{M})\mathbf{M}$$

The fourth algorithm is analogous, but with $\mathbf{F}_{\text{def}}^{\text{RK2}}$ replaced by $\mathbf{F}_{\text{orth}}^{\text{RK2}}$ and σ_{def} replaced by an appropriate function σ_{orth} . (The function σ_{orth} is a rational function in m and the components of \mathbf{A} , but is significantly more complicated than σ_{def} .) Note that isotropy plays a role both in the choice of the generator and in the selection of a correction term.

4.4 Fourth order methods

In this subsection, we describe two families of fourth order Lie group integrators on \mathcal{M} . We emphasize that these algorithms map a point $\mathbf{M}_n \in \mathcal{M}$ *exactly* into \mathcal{M} ; they are fourth order accurate in the sense that they approximate the true trajectories within \mathcal{M} to fourth order. A direct implementation of the classic fourth-order Runge–Kutta method to a vector field on \mathcal{M} fails to map exactly into the manifold \mathcal{M} , while application of the classical RK4 method to the generator of the flow, followed by application of the exponential map and the group action necessarily yields an update in \mathcal{M} , but typically does not give a fourth order approximation of the true flow. The generator must be modified to account for the trivialization of the tangent bundle of the group; this modification can be implemented either before or after the stages of the Runge–Kutta method are computed and averaged. The first method we use is the RKMK4 method, a Runge–Kutta style method due to Munthe–Kaas ([39], [40]) in which each stage of a traditional RK4 method is modified so that the resulting generator, followed by (algorithmic) exponentiation and application of the group action to the manifold, yields a fourth order method. The second method utilizes a series expansion of the generator along the true flow, followed by a single modification to account for the trivialization of the tangent bundle of the group \mathcal{G} , again followed by (algorithmic) exponentiation and application of the group action.

We implemented the RKMK4 method [39], using the Cayley transform rather than the true matrix exponential. To implement a Lie group integrator for (8) using the Cayley transform, we make use of the fact that, for sufficiently small t , there is a function $\mathbf{f} : \mathbb{R} \rightarrow \mathbb{R}^3$ satisfying

$$\mathbf{M}(t) = \text{cay}(\mathbf{f}(t))\mathbf{M}(0). \quad (24)$$

Differentiating (24) with respect to t , we obtain

$$\begin{aligned} \dot{\mathbf{M}}(t) &= \text{dcay}_{\mathbf{f}}(\mathbf{f}'(t)) \times \text{cay}(\mathbf{f}(t))\mathbf{M}(0) \\ &= \text{dcay}_{\mathbf{f}}(\mathbf{f}'(t)) \times \mathbf{M}(t) \\ &= \mathbf{A}(\mathbf{M}(t)) \times \mathbf{M}(t), \end{aligned}$$

where the map $\text{dcay}_{\mathbf{f}} = \tilde{D}\text{cay}(\mathbf{f}) : \mathbb{R}^3 \rightarrow \mathbb{R}^3$ is the right trivialization of the tangent map of the Cayley transform.

Hence \mathbf{f}' and \mathbf{A} are related by

$$\text{dcay}_{\mathbf{f}}(\mathbf{f}'(t)) \times \mathbf{M}(t) = \mathbf{A}(\mathbf{M}(t)) \times \mathbf{M}(t),$$

which is equivalent to

$$\mathbf{f}'(t) = \text{dcay}_{\mathbf{f}}^{-1}(\mathbf{A}(\mathbf{M}(t)) + \sigma(t)\mathbf{M}(t)) \quad (25)$$

for some function σ . The initial condition for (24) is $\mathbf{f}(0) = 0$.

The map $\text{dcay}_{\mathbf{f}} : \mathbb{R}^3 \rightarrow \mathbb{R}^3$ satisfies

$$\text{dcay}_{\mathbf{f}} := \frac{1}{1 + \|\frac{1}{2}\mathbf{f}\|^2} (I + \frac{1}{2} \text{skew}[\mathbf{f}])$$

and

$$\text{dcay}_{\mathbf{f}}^{-1} = I - \frac{1}{2} \text{skew}[\mathbf{f}] + \frac{1}{4} \mathbf{f} \mathbf{f}^T.$$

The Cayley version of the RKMK4 method is essentially the conventional RK4 applied to (25): having found \mathbf{M}_n at time t_n , we construct the update

$$\mathbf{M}_{n+1} = \mathbf{M}(t_n + \Delta t) = \text{cay}(\mathbf{F}^{RK4}(\mathbf{M}_n, \Delta t)) \mathbf{M}_n,$$

where

$$\mathbf{F}^{RK4}(\mathbf{M}_n, \Delta t) = \frac{1}{6}(\mathbf{F}_1 + 2\mathbf{F}_2 + 2\mathbf{F}_3 + \mathbf{F}_4)$$

and

$$\begin{aligned} \mathbf{A}_1 &= \Delta t \mathbf{A}(\mathbf{M}_n), & \mathbf{F}_1 &= \text{dcay}_{\mathbf{0}}^{-1}(\mathbf{A}_1) \\ \mathbf{A}_2 &= \Delta t \mathbf{A}(\text{cay}(\frac{1}{2}\mathbf{A}_1) \mathbf{M}_n), & \mathbf{F}_2 &= \text{dcay}_{\frac{1}{2}\mathbf{A}_1}^{-1}(\mathbf{A}_2) \\ \mathbf{A}_3 &= \Delta t \mathbf{A}(\text{cay}(\frac{1}{2}\mathbf{A}_2) \mathbf{M}_n), & \mathbf{F}_3 &= \text{dcay}_{\frac{1}{2}\mathbf{A}_2}^{-1}(\mathbf{A}_3) \\ \mathbf{A}_4 &= \Delta t \mathbf{A}(\text{cay}(\mathbf{A}_3) \mathbf{M}_n), & \mathbf{F}_4 &= \text{dcay}_{\mathbf{A}_3}^{-1}(\mathbf{A}_4) \end{aligned}$$

For more details on this method, see [39].

The second method involves a series expansion with respect to time of the generator $\mathbf{A}(\mathcal{F}_t(\mathbf{M}))$, where \mathcal{F}_t denotes the exact flow at time t . Given the generator \mathbf{A} , this expansion is computed by iteratively symbolically differentiating $\mathbf{A}(\mathcal{F}_t(\mathbf{M}))$ and then substituting $\mathbf{A}(\mathbf{M}) \times \mathbf{M}$ for $\dot{\mathbf{M}}$. The third order approximation to $\mathbf{A}(\mathcal{F}_t(\mathbf{M}))$ is then modified to take into account the trivialization of the tangent bundle of $SO(3)$ and the action of $SO(3)$ on S^2 . The specific expressions for this modification for the rigid body equations on the sphere are given in §5. Given the implicit and highly nonlinear nature of the LLG equations, symbolic calculation of the derivatives of \mathbf{A} for this system seemed excessively complicated; hence we did not implement this algorithm for the LLG system.

5 An example: the rigid body flow on a sphere

We now apply the results outlined above to a simple and familiar system, the reduced rigid body equations on the sphere. Given a positive definite symmetric three by three matrix \mathbb{I} , define the vector field

$$X(m) = m \times \mathbb{I}^{-1}m \tag{26}$$

on S^2 . This is a Hamiltonian system with respect to the Kostant–Kirillov–Souriau symplectic structure

$$\Omega(m)(\xi \times m, \eta \times m) = \langle m, \xi \times \eta \rangle$$

and Hamiltonian

$$H(m) = \frac{1}{2} \langle m, \mathbb{I}^{-1}m \rangle. \tag{27}$$

The system (26) is the symplectic reduction of the free rigid body equations on $T^*SO(3)$; more concretely, it is the restriction of Euler’s equation for the body angular momentum to the unit sphere. (Since the norm of the body momentum is preserved by the dynamics of Euler’s equation, all spheres centered at the origin are invariant submanifolds.) The conservative nature of this system makes it particularly easy to measure the error in orbit capture; if the body is triaxial, i.e. the eigenvalues I_1, I_2, I_3 of the inertia tensor \mathbb{I} are distinct, the level sets of the Hamiltonian (27) exactly determine the orbits of the system. Thus in this situation the error in the orbit is a function of the fluctuation in the energy. As the numerical results given in tables 1–4 demonstrate, geometric integration techniques yield efficient, accurate orbit capture for the reduced free rigid body, with good performance even for very large time steps. Note that the same randomly generated initial conditions and inertia tensors are used in all of the numerical simulations.

If the rigid body is axisymmetric, then all true trajectories consist either of equilibria (the ‘poles’ and the ‘equator’) or of steady rotations in the plane of symmetry. Note that in this situation, even an exactly energy-preserving scheme may allow drift across the family of one-point orbits along the equator. However, all of the methods considered here detect equilibria as such. Thus even in the axisymmetric case, we can use the energy to monitor orbit capture. We shall see that for some of the algorithms considered here, there are significant differences in performance on triaxial and axisymmetric bodies. Symmetries play a crucial role in algorithm design and analysis; see, e.g. [43]. However, we shall not explore those issues in any detail here.

5.1 Euler methods for rigid body dynamics

We now consider implementations of the families of algorithms described in §4 for the rigid body equations. We take as our default generator the body angular velocity $A(m) = \mathbb{I}^{-1}m$. We first consider three first order methods, with infinitesimal updates

- $F_{\text{def}}^{\text{Eul}}(m) = \mathbb{I}^{-1}m$
- $F_{\text{orth}}^{\text{Eul}}(m) = \mathbb{I}^{-1}m - \langle m, \mathbb{I}^{-1}m \rangle m = A(m) - 2H(m)m$
- $F_{\text{cor}}^{\text{Eul}}(m) = \mathbb{I}^{-1}m - \frac{\langle X(m), \mathbb{I}^{-1}X(m) \rangle}{\|X(m)\|^2} m = \mathbb{I}^{-1}m + \frac{\tau(u(m))}{\tau(\mathbb{I}u(m))} m,$

where $\tau : \mathbb{R}^3 \rightarrow \mathbb{R}$ and $u : S^2 \rightarrow \mathbb{R}^3$ are given with respect to an eigenbasis of \mathbb{I} by

$$\tau(\mathbf{x}) = x_1 + x_2 + x_3 \quad \text{and} \quad u(m)_i := (I_j - I_k)^2 I_i m_j m_k$$

for any cyclic permutation (i, j, k) of $(1, 2, 3)$.

	$F_{\text{def}}^{\text{Eul}}$	$F_{\text{orth}}^{\text{Eul}}$	$F_{\text{cor}}^{\text{Eul}}$
Triaxial	$6.37 \cdot 10^{-2}$	$2.23 \cdot 10^{-2}$	$4.60 \cdot 10^{-6}$
Axisymmetric	$2.46 \cdot 10^{-1}$	$1.46 \cdot 10^{-1}$	$7.38 \cdot 10^{-14}$

Table 1: Maximum energy error over the trajectories given in figure 5.1.

Δt	Triaxial			Axisymmetric		
	$F_{\text{def}}^{\text{Eul}}$	$F_{\text{orth}}^{\text{Eul}}$	$F_{\text{cor}}^{\text{Eul}}$	$F_{\text{def}}^{\text{Eul}}$	$F_{\text{orth}}^{\text{Eul}}$	$F_{\text{cor}}^{\text{Eul}}$
10	$9.04 \cdot 10^{-2}$	$1.81 \cdot 10^{-2}$	$4.56 \cdot 10^{-3}$	$7.66 \cdot 10^{-3}$	$8.37 \cdot 10^{-4}$	0.00
1	$8.52 \cdot 10^{-2}$	$8.54 \cdot 10^{-3}$	$3.68 \cdot 10^{-5}$	$1.79 \cdot 10^{-3}$	$1.13 \cdot 10^{-4}$	0.00
.1	$9.06 \cdot 10^{-3}$	$1.44 \cdot 10^{-3}$	$3.55 \cdot 10^{-7}$	$2.51 \cdot 10^{-4}$	$1.17 \cdot 10^{-5}$	0.00
.01	$7.09 \cdot 10^{-4}$	$1.62 \cdot 10^{-4}$	$3.57 \cdot 10^{-9}$	$2.96 \cdot 10^{-5}$	$1.18 \cdot 10^{-6}$	0.00

Table 2: Average global energy errors over ten sample runs with randomly generated initial conditions and inertia tensors, integrated over the interval $[0, 100]$ using versions of the forward Euler method.

In table 2 we provide the average maximum errors in the energy for time steps $\Delta t = 10, 1, .1,$ and $.01,$ using for ten randomly generated initial conditions and inertia tensors each for triaxial and axisymmetric bodies.

The separatrix is exactly captured if the infinitesimal updates $F_{\text{orth}}^{\text{Eul}}$ or $F_{\text{cor}}^{\text{Eul}}$, which coincide on the separatrix, are used. On the other hand, when $F_{\text{def}}^{\text{Eul}}$ was used to integrate ten sample trajectories with

Figure 1: Sample trajectories computed over the interval $[0, 200]$ using the time step $\Delta t = 0.1$ and, left to right, the first order infinitesimal updates $F_{\text{def}}^{\text{Eul}}$, $F_{\text{orth}}^{\text{Eul}}$, and $F_{\text{cor}}^{\text{Eul}}$. The upper row is computed using the inertia tensor of a triaxial rigid body, while the lower row is computed for an axisymmetric rigid body.

initial conditions at random points on the separatrices of rigid bodies with randomly generated inertia tensors, the average errors over the integration interval $[0, 500]$ were: $9.72 \cdot 10^{-2}$ for $\Delta t = 1$, $3.89 \cdot 10^{-2}$ for $\Delta t = .1$, and $1.94 \cdot 10^{-3}$ for $\Delta t = .01$.

In the axisymmetric case, the forward Euler method with infinitesimal update $F_{\text{cor}}^{\text{Eul}}$ associated to second order orbit approximation yields the exact solution when the true exponential map is used as the algorithmic exponential. (If the Cayley transform is used as the algorithmic exponential, then the orbits are captured exactly, but the algorithmic trajectories differ from the true trajectories by a time reparametrization.) Note that the ‘default’ generator and the orthogonal generator yield only first order orbit approximations even in the axisymmetric case.

As implemented in our *Mathematica* code, the version of the forward Euler method with orthogonal algorithmic velocity is approximately 10% slower than the naive version, while the version that captures orbits to second order is approximately 30% slower than the naive version.

5.2 Higher order methods for rigid body dynamics

Triaxial				
Δt	$F_{\text{def}}^{\text{RK2}}$	$F_{\text{orth}}^{\text{RK2}}$	$F_{\text{dcor}}^{\text{RK2}}$	$F_{\text{ocor}}^{\text{RK2}}$
10	$7.22 \cdot 10^{-2}$	$1.22 \cdot 10^{-2}$	$6.11 \cdot 10^{-2}$	$4.99 \cdot 10^{-2}$
1	$4.36 \cdot 10^{-3}$	$1.06 \cdot 10^{-4}$	$9.61 \cdot 10^{-4}$	$5.67 \cdot 10^{-7}$
.1	$5.03 \cdot 10^{-6}$	$1.10 \cdot 10^{-7}$	$1.11 \cdot 10^{-8}$	$2.14 \cdot 10^{-11}$
.01	$5.01 \cdot 10^{-9}$	$1.10 \cdot 10^{-10}$	$2.94 \cdot 10^{-13}$	$9.07 \cdot 10^{-15}$
Axisymmetric				
Δt	$F_{\text{def}}^{\text{RK2}}$	$F_{\text{orth}}^{\text{RK2}}$	$F_{\text{dcor}}^{\text{RK2}}$	$F_{\text{ocor}}^{\text{RK2}}$
10	$6.57 \cdot 10^{-3}$	$2.27 \cdot 10^{-5}$	$5054 \cdot 10^{-3}$	$8.37 \cdot 10^{-7}$
1	$1.22 \cdot 10^{-4}$	$2.44 \cdot 10^{-8}$	$1.22 \cdot 10^{-5}$	$9.09 \cdot 10^{-12}$
.1	$1.75 \cdot 10^{-7}$	$2.46 \cdot 10^{-11}$	$1.27 \cdot 10^{-10}$	$3.15 \cdot 10^{-16}$
.01	$1.75 \cdot 10^{-10}$	$2.74 \cdot 10^{-14}$	$6.61 \cdot 10^{-16}$	$3.79 \cdot 10^{-15}$

Table 3: Average global energy errors over ten sample runs with randomly generated initial conditions and inertia tensors, integrated over the interval $[0, 100]$ using versions of the Heun method.

We implemented the four different versions of the Heun method given in section 4.3 for the rigid body system. Although the Heun methods $F_{\text{def}}^{\text{RK2}}$ and $F_{\text{orth}}^{\text{RK2}}$ described here are only second order accurate, the (local) discretization error in the energy is fourth order in the time step.

The isotropy corrected versions used here take the form

$$F_{\text{dcor}}^{\text{RK2}}(m, \Delta t) := F_{\text{def}}^{\text{RK2}}(m, \Delta t) + \Delta t^3 \sigma_{\text{def}}(m)m,$$

where

$$\sigma_{\text{def}}(m) := \frac{\langle J^n, u \rangle}{\langle J^d, u \rangle}, \quad \text{with} \quad \begin{cases} u_j := (m_k m_\ell)^2 \\ J_j^n := -I_j(I_k + I_\ell)(I_k - I_\ell)^2 \\ J_j^d := 4 I_1 I_2 I_3 I_j^2 (I_k - I_\ell)^2 \end{cases}$$

for any cyclic permutation (j, k, ℓ) of $(1, 2, 3)$ and

$$F_{\text{ocor}}^{\text{RK2}}(m, \Delta t) := F_{\text{orth}}^{\text{RK2}}(m, \Delta t) + \Delta t^3 \sigma_{\text{orth}}(m)m,$$

where σ_{orth} is another, significantly more complicated, rational function in m and the components of the inertia tensor. The isotropy corrections σ_{def} and σ_{orth} given above determine algorithms yielding fourth order

Triaxial						
Δt	$F_{\text{def}}^{\text{sy}4}$	$F_{\text{orth}}^{\text{sy}4}$	$F_{\text{dcor}}^{\text{sy}4}$	$F_{\text{ocor}}^{\text{sy}4}$	$F_{\text{def}}^{\text{RK}4}$	$F_{\text{orth}}^{\text{RK}4}$
10	$5.72 \cdot 10^{-3}$	$3.37 \cdot 10^{-2}$	$6.06 \cdot 10^{-3}$	$1.90 \cdot 10^{-2}$	$6.07 \cdot 10^{-2}$	$3.59 \cdot 10^{-3}$
1	$3.62 \cdot 10^{-6}$	$2.72 \cdot 10^{-7}$	$1.55 \cdot 10^{-6}$	$1.68 \cdot 10^{-7}$	$2.15 \cdot 10^{-5}$	$1.46 \cdot 10^{-7}$
.1	$3.56 \cdot 10^{-10}$	$7.45 \cdot 10^{-12}$	$3.61 \cdot 10^{-10}$	$1.70 \cdot 10^{-12}$	$2.97 \cdot 10^{-10}$	$3.06 \cdot 10^{-12}$
Axisymmetric						
Δt	$F_{\text{def}}^{\text{sy}4}$	$F_{\text{orth}}^{\text{sy}4}$	$F_{\text{dcor}}^{\text{sy}4}$	$F_{\text{ocor}}^{\text{sy}4}$	$F_{\text{def}}^{\text{RK}4}$	$F_{\text{orth}}^{\text{RK}4}$
10	$2.47 \cdot 10^{-4}$	$1.24 \cdot 10^{-7}$	$2.47 \cdot 10^{-4}$	$1.24 \cdot 10^{-7}$	$7.45 \cdot 10^{-4}$	$4.41 \cdot 10^{-8}$
1	$2.06 \cdot 10^{-8}$	$1.26 \cdot 10^{-12}$	$2.06 \cdot 10^{-8}$	$1.26 \cdot 10^{-12}$	$3.20 \cdot 10^{-7}$	$4.47 \cdot 10^{-13}$
.1	$2.12 \cdot 10^{-13}$	0.00	$2.12 \cdot 10^{-13}$	0.00	$3.47 \cdot 10^{-12}$	$3.22 \cdot 10^{-16}$

Table 4: Average global energy errors over ten sample runs with randomly generated initial conditions and inertia tensors, integrated over the interval $[0, 100]$ using several fourth order methods.

energy capture. If the body is axisymmetric, $F_{\text{dcor}}^{\text{RK}2}$ preserves the energy to fifth order. As Table 3 shows, some of these algorithms appear to have better *global* energy capture than the single step discretization energy error analysis (which we carried out symbolically using *Mathematica*) would suggest. Plots of the energy errors in the sample integrations, with randomly generated initial conditions and inertia tensors, show that the energy oscillates about a very slow drift away from the correct value. Note that the energy correction term for the fourth order symbolic expansion method using the orthogonal generator is identically zero if the body is axisymmetric; hence the results generated by $F_{\text{orth}}^{\text{sy}4}$ and $F_{\text{ocor}}^{\text{sy}4}$ coincide in this case.

We consider six fourth order geometric methods. Four utilize a series expansion for the generator along a solution curve, while the other two use the RKMK4 algorithm (with the Cayley transform as the algorithmic exponential). Using the Cayley transform, the map $F_{\text{def}}^{\text{sy}4}$ determined by the default generator for the rigid body system on S^2 is given by

$$F_{\text{def}}^{\text{sy}4}(m, \Delta t) = \sum_{j=1}^4 \frac{\Delta t^j}{j!} A^{(j-1)}(m) + \frac{\Delta t^3}{12} \left(\|A(m)\|^2 A(m) + \dot{A}(m) \times A(m) \right) + \frac{\Delta t^4}{4!} \left(\|A(m)\|^2 \dot{A}(m) + \ddot{A}(m) \times A(m) + 2 \langle \dot{A}(m), A(m) \rangle A(m) \right),$$

where $A^{(j)}(m) = \frac{\partial^j}{\partial t^j} A(\mathcal{F}_t(m))|_{t=0}$. The corresponding algorithm for the rigid body using the orthogonal generator is

$$F_{\text{orth}}^{\text{sy}4}(m, \Delta t) = \sum_{j=1}^4 \frac{\Delta t^j}{j!} A_o^{(j-1)}(m) + \frac{\Delta t^3}{12} \left(\|A_o(m)\|^2 A_o(m) + \langle \ddot{A}_o(m), m \rangle m \right) + \frac{\Delta t^4}{8} \langle \dot{A}_o(m), A_o(m) \rangle A_o(m).$$

The infinitesimal updates $F_{\text{def}}^{\text{sy}4}$ and $F_{\text{orth}}^{\text{sy}4}$ can be modified by the addition of an appropriate multiple of the argument m to yield an additional order of energy, and hence orbit, capture. The scalar correction functions, which are rational functions of the components of m and the inertia tensor, were determined by symbolic calculation.

6 Application of geometric integration to numerical micromagnetics

In this section, the geometric integrators developed in section 4 are applied to the Landau-Lifshitz-Gilbert equations of micromagnetics. The exact solution of this system is typically not available to us; indeed, it is the lack of precise analytical results for comparison which makes numerical micromagnetics a challenging field. In our examples, we chose the largest possible time steps for a given method that would lead the system to the solution computed by a higher order method (within prescribed tolerance).

As mentioned earlier, numerical micromagnetics has attracted much attention in the mathematical community, for several reasons. In this paper we are focussing on the time-stepping aspect of the problem. The application of geometric integration techniques in this context is relatively new, see for example, [44, 45]. Recently, another technique which modifies existing integrators was developed for numerical micromagnetics, [51]. This new integrator is of the “step-and-project” class, but is stable.

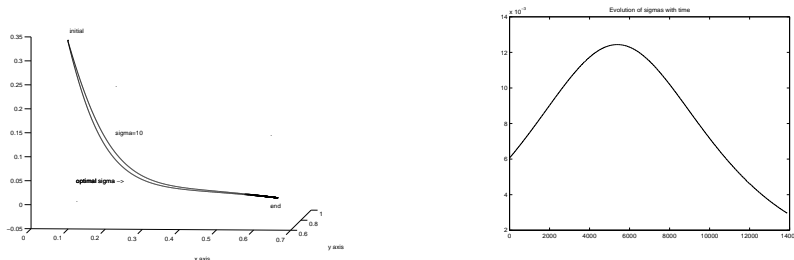


Figure 2: *The trajectories followed by the usual forward Euler $\Delta t = 0.0001$ and with the geometric forward Euler ($\Delta t = 0.01$) with optimal σ are almost identical; if we assume $\sigma = 10$ (an arbitrary choice), the trajectory precesses more before reaching the final point. The figure on the right shows the evolution of the optimal σ . The applied field is uniform and weak, specifically, $\mathbf{H}_{\text{app}} = (0.05, 0.05, 0)$.*

We were particularly interested in the behavior of the free parameter σ which appears in the geometric time-stepping algorithm (11). In the rigid body case the parameter can be chosen to improve energy conservation. Here the system is dissipative and a criterion for the selection of σ is not immediately obvious. For the forward Euler implementation, we can derive a relatively simple expression for a function σ that minimizes the discretization error. For higher order methods, analogous functions can be described in terms of the series expansions of the true and algorithmic flows, but the cost of computing these expansions, particularly for systems such as the LLG equations, rapidly becomes prohibitive. Work is in progress to determine computationally tractable criteria for the selection of the isotropy component for higher order methods.

6.1 Description of the model problem

We describe a model problem for the LLG, for which the analytical solution was particularly simple. Recall that the LLG for the magnetization $\boldsymbol{\mu}(x, t)$ is given by (2), which we recall here for convenience:

$$\frac{\partial}{\partial t} \boldsymbol{\mu} = -\boldsymbol{\mu} \times \mathbf{H}_{\text{eff}}(\boldsymbol{\mu}) - \lambda \boldsymbol{\mu} \times (\boldsymbol{\mu} \times \mathbf{H}_{\text{eff}}(\boldsymbol{\mu})), \quad \|\boldsymbol{\mu}(\mathbf{x})\| = 1 \quad \forall \mathbf{x} \in \mathcal{B}. \quad (28)$$

$$\mathbf{H}_{\text{eff}}(\boldsymbol{\mu}) = A\Delta\boldsymbol{\mu} + \mu_0(-\nabla\phi + \mathbf{H}_{\text{app}}) + K(\boldsymbol{\mu} \cdot \mathbf{e})\mathbf{e}. \quad (29)$$

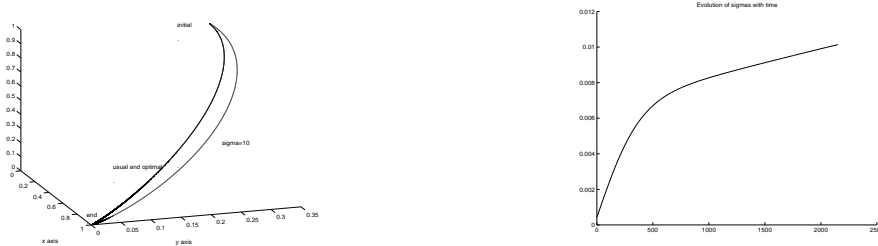


Figure 3: *The evolution of one point in the ferromagnetic sample. The trajectories followed by the usual forward Euler method with time step $\Delta t = 0.0001$ and by the geometric forward Euler method with optimal σ and time step $\Delta t = 0.01$ are almost identical; if we set $\sigma \equiv 10$ (an arbitrary choice) in the geometric forward Euler method, the trajectory precesses more before reaching the final point. The figure on the right shows the evolution of the optimal σ . The applied field is uniform, $\mathbf{H}_{\text{app}} = (5, 0, 0)$.*

In the experiments that follow, we set $\mu_0 = K = A = 1.0$ and vary the applied field. These parameter values are not taken from actual physical data, and were selected solely for purposes of illustration. The saturation magnetization was $\|\boldsymbol{\mu}(\mathbf{x})\| \equiv 1$.

We wish to construct a one-dimensional example where the computation of the demagnetizing energy would be simple. To this end, we assume the sample is contained in the infinite slab $\{(x, y, z) | 0 \leq x \leq 1, y, z, \in \mathbb{R}^1\}$. We assume the magnetization $\boldsymbol{\mu} = \boldsymbol{\mu}(x)$, ie., the only variation in the magnetization is along the x-direction. Therefore, $\nabla \cdot \boldsymbol{\mu} = (\frac{\partial}{\partial x} \mu_1, 0, 0)$. We assume that there are 100 individual spins uniformly distributed along $x \in [0, 1]$. These spins interact with each other through the exchange and demagnetizing fields.

This example is admittedly a simplistic one; the true equilibrium solution for it can easily be found using analytical techniques. Therefore, the stopping criterion used was a comparison with the exact final equilibrium point. We see that the geometric integrators take trajectories which respect the point-wise constraints on the magnetization; conventional integrators do not. Thus, the paths traversed by these integrators will be different, as is seen in figures 2 and 3. As the step-size is shrunk more and more, the trajectories will converge.

6.2 A first order method for the LLG

In the first set of numerical experiments, we implemented the geometrical analog of the forward Euler algorithm for the LLG equation. We then tracked the evolution of the parameter σ given by (22), an expression derived through arguments of discretization error minimization. We approximated the acceleration $\dot{\mathbf{M}}_n$ of trajectories $\mathbf{M}(t)$ of (8) using a one-sided discrete approximation of the derivative of $\dot{\mathbf{M}}_n = \mathbf{A}(\mathbf{M}_n) \times \mathbf{M}_n$.

Figures 2 and 3 describe the trajectories followed by the over-damped LLG system (without the Larmor precession term) for two different applied fields. To address the issue of overall computational expense, we ran both a geometric forward Euler algorithm and the conventional forward Euler algorithm on the example introduced above. For each algorithm, we decreased the time step Δt until the trajectories converged to within 5%. We also required that the final equilibrium point corresponded to that computed by a fourth-order Runge-Kutta method with time step $\Delta t = 0.0001$, to within a relative error of 1%. The geometric forward Euler method yielded trajectories which converged, for this example, with time steps of $\Delta t = 0.01$ and a CPU time of 1.77 seconds. The usual forward Euler required a time step $\Delta t = 0.0001$, with a CPU time of 3.88 seconds, to get similar behaviour. In addition, while the pointwise norm of \mathbf{M} was conserved to machine accuracy by the geometric integrator, the standard forward Euler algorithm caused $\|\mathbf{M}\|$ to increase to 1.001183806 times its usual value by the end of the run. As a consequence, the trajectories traversed by the geometric and the usual algorithms differed, though they ended at the nearly same place. As we are only interested in the final equilibrium state of the system, we see the obvious merit of using the geometric integrator — we can obtain accurate final states while using much larger time steps.

We see the effect of varying the scalar functions σ on the trajectories is that of changing the amount of precession in the trajectory. We notice certain trends in the optimally chosen function $\sigma(t)$ in figures 2 and 3, and we shall investigate the relationship of these trends to the physical processes occurring at the same times in future work.



Figure 4: An example of the full LLG system, with uniform applied field $\mathbf{H}_{\text{app}} = (5, 0, 0)$ and damping parameter $\lambda = 0.05$. The trajectories were computed using the usual forward Euler method with time step $\Delta t = 0.0001$ and the geometric forward Euler method with time step $\Delta t = 0.01$. Here the trajectory taken by the geometric method differs appreciably from those of the usual method, though the final states appear to be similar. The lefthand plot shows the evolution of one point in the ferromagnetic sample; the righthand plot shows the evolution of the optimal sigma at that point.

In figure 4, we implemented the code for the full LLG system, including the Larmor precession. The applied field is uniform, $\mathbf{H}_{\text{app}} = (5, 0, 0)$. The damping parameter λ was set to a low value, specifically $\lambda = 0.05$. The trajectories followed by the usual forward Euler and $\Delta t = 0.0001$ and by the geometric forward Euler with $\Delta t = 0.01$ and optimal σ diverge appreciably, yet end at the same final state. The drift of the norm is now clearly visible (see figure (5)). The usual forward Euler trajectory moves off the unit sphere in the standard Euler integration, while the geometrically integrated one does not. We see that the optimal σ now varies more (figure 4b).

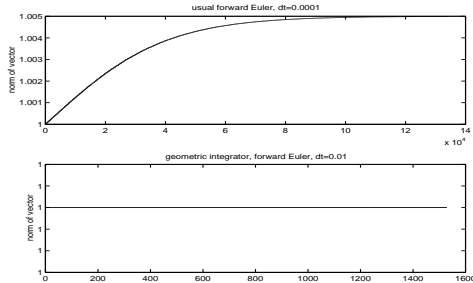


Figure 5: Norm of magnetization in Fig(3). The geometric integrator exactly preserves the norm, even with a time step of 0.01. The usual forward Euler method shows a drift in norm, even with a time step of 0.0001.

6.3 A second order method for micromagnetics

In the next set of experiments, we implemented the geometrical versions of the Heun algorithm, derived in section 4. We did not have an analytical expression for the optimal choice of σ . Therefore, we ran the experiments for several constant values of this parameter, and computed the order of convergence of the algorithm in Δt .

The results were interesting, and rather striking. As σ is varied, the order of convergence changes for the naive choice of generator. What should be noted is that the geometric algorithm appears to converge more rapidly than a conventional Heun method; the order of convergence was $O(\Delta t^{2+\delta})$, as was borne out in repeated experiments.

The norm of \mathbf{M} is conserved to machine precision for both generators.

6.4 A fourth order method for micromagnetics: RKMK4

We now present experiments with a fourth order method derived in section 4. Lacking an analytical expression for the optimal choice of σ , we ran the experiments for varying constant values of this parameter, and computed the order of convergence of the algorithm in Δt .

In figure 8 we track $\|\mathbf{M}\|$ over $[0, 1]$ with a time step of 0.01. The classical RK4 method without projection shows a drift in the norm; this drift is of the order of 10^{-6} , i.e., $O(\Delta t^3)$. The Lie group integrator, on the other hand, shows no drift (up to machine precision).

As we vary σ , we observe that the rate of convergence of the algorithm varies, see (figure 9). Again, there is clearly some optimal value of this parameter. This behavior is even more pronounced for the RKMK4

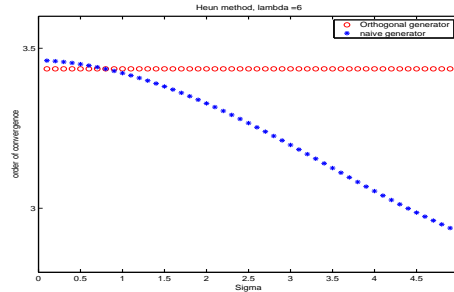


Figure 6: *Convergence orders of the Heun method for varying σ . We show experiments corresponding to two different generators.*

method than for the Heun method.

Acknowledgements: The authors would like to thank the referees for their insightful and helpful suggestions. We also thank the Institute for Mathematics and its Applications, where the bulk of this research was conducted.

References

- [1] M. Fels, P. Olver, Moving coframes. I. A practical algorithm, *Acta Appl. Math* 51 (1998) 161–213.
- [2] M. Fels, P. Olver, Moving coframes. II. Regularization and theoretical foundations, *Acta Appl. Math.* 55 (1999) 127–208.
- [3] D. Lewis, P. Olver, Geometric integration algorithms on homogeneous manifolds, *Foundations of Computational Mathematics* To appear.
- [4] D. Lewis, N. Nigam, P. Olver, Connections for nonfree group actions, preprint. (2001).
- [5] R. de Vogelaère, Methods of integration which preserve the contact transformation property of the Hamiltonian equations, *Tech. rep.* (1956).
- [6] F. J. Dragt, A.J., Norm form for mirror machine Hamiltonians, *J. Math. Phys.* 20 (1979) 2649–2660.
- [7] A. Veselov, Integrable discrete-time systems and difference operators, *Funkts. Anal. Prilozhen* 22 (1988) 1–13.

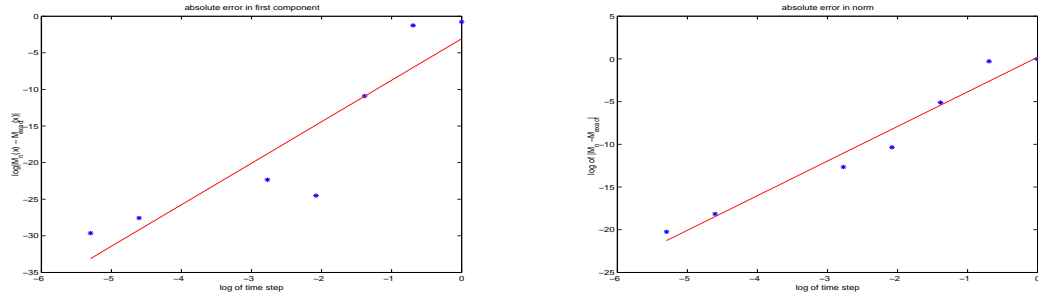


Figure 7: On the left: Error in the first component of \mathbf{M} as a function of time step, $\sigma = 0$. Here we see $O(\Delta t^{5.6})$ convergence. On the right: Norm of the error of \mathbf{M} as a function of time step, with $\sigma = 0$. Here we see $O(\Delta t^{4.03})$ convergence.

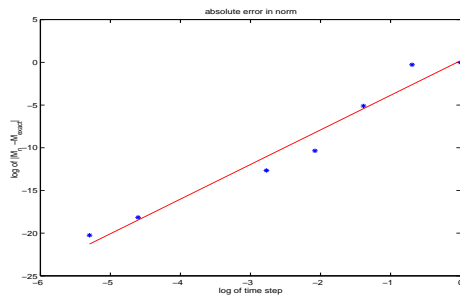


Figure 8: $\text{Log}(\text{norm})$ of the magnetization over the integration interval

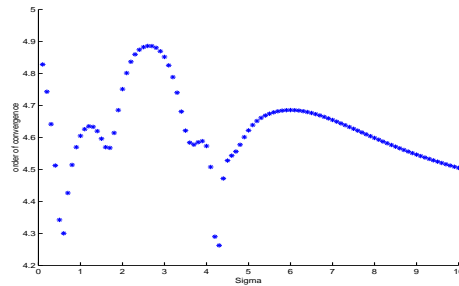


Figure 9: *Order of convergence of the algorithm as a function of σ , with damping parameter $\lambda = 10$.*

- [8] N. Nigam, Joint IMA-Seagate project on numerical micromagnetics, Tech. rep., IMA and Seagate technologies (May 2001).
- [9] S. Parkin, The magic of multilayers, Tech. Rep. 1, IBM, vol 42 (1998).
- [10] A. Iraqi, et al., Functionalisation of poly(p-phenylenevinylene) polymers with pendant nitroxide groups”, Synthetic Metals .
- [11] F. Alouges, A new algorithm for computing liquid crystal stable configurations: the harmonic mapping case, SIAM J. Numer. Anal. 34 (5) (1997) 1708–1726.
- [12] P.Kollman, Free energy calculations: Applications to Chemical and Biochemical phenomena, Chem. Rev. 93 (1993) 2395–2417.
- [13] Y. Wang, K. Kuczera, Exploration of free energy surfaces of helical Ala and Aib peptide, J. Phys. Chem. B. 101 (1997) 5205–5213.
- [14] B. Dieny, et al., Magnetotransport properties of magnetically soft spin-valve structure, J. Appl. Physics 69 (1991) 4774–4779.
- [15] W. Brown, Micromagnetics, New York Interscience, 1963.
- [16] A. Aharoni, Introduction to the theory of ferromagnetism, in: Monographs on Physics, Oxford University Press, 1996.
- [17] T. Gilbert, A Lagrangian formulation of gyromagnetic equation of the magnetization field, Phys. Rev. 100.
- [18] L. Landau, E. Lifshitz, On the theory of magnetic permeability in ferromagnetic bodies, Physik. Z. Sowjetunion 8.
- [19] D. Lewis, E. Della Torre, Identification of stiff modes in micromagnetics problems, IEEE Trans. Magn. 33 (1997) 1596–1599.

- [20] V. D. Tsiantos, D. Suess, T. Schrefl, J. Fidler, Stiffness analysis for the micromagnetic standard problem No. 4, *J. Appl. Phys.* 89 (2001) 7600–7602.
- [21] M. J. Donahue, D. G. Porter, R. D. McMichael, J. Eicke, Behaviour of muMAG standard problem No. 2 in the small particle limit, *J. Appl. Phys.* 87 (2000) 5520–5522.
- [22] M. J. Donahue, R. D. McMichael, Exchange energy representations in computational micromagnetics, *Physica B* 233 (1997) 272–278.
- [23] W. Scholz, Micromagnetic simulation of thermally activated switching in fine particles, Ph.D. thesis, Institut für Angewandte und Technische Physik der Technischen Universität Wien (1999).
- [24] B. Yang, D. Fredkin, Dynamical micromagnetics by the finite element method, *IEEE Trans. Magnetics* 34 (1998) 3842–3852.
- [25] J. Oti, Numerical micromagnetic techniques and their applications to magnetic force microscopy calculations, *IEEE Trans. Magnetics* 29 (1993) 2359–2364.
- [26] S. Polstyanko, G. Peng, J.-F. Lee, Algebraic multigrid method for solving FEM matrix equations for 3d static problems, *IEEE Trans. Magnetics* 35 (1999) 1183–1186.
- [27] I. Tsukerman, Fast finite element solvers for problems with magnetic materials, *IEEE Trans. Magnetics* 29 (1993) 2365–2367.
- [28] P. Monk, O. Vacus, Accurate discretization of a nonlinear micromagnetic problem (June 1999).
- [29] A. Aharoni, Magnetostatic energy calculations, *IEEE Trans. Magnetics* 27 (1991) 3537–3547.
- [30] A. Aharoni, Critique on the numerical micromagnetics of nano-particles, *J. Magn. Mag. Mat.* 203 (1999) 33–36.
- [31] P. Asselin, A. Thiele, On the field Lagrangians in micromagnetics, *IEEE Trans. Magnetics* 22 (1986) 1876–1880.
- [32] D. Fredkin, T. Koehler, Ab initio micromagnetic calculations for particles, *J. Appl. Phys.* 67 (1990) 5544–5548.
- [33] M. Luskin, L. Ma, Numerical optimization of the micromagnetics energy, in: *Proceedings of the Session on Mathematics in Smart Materials, SPIE 1993 Conference on Smart Structures*, 1993.
- [34] T. Schrefl, J. Fidler, Numerical micromagnetics in hard magnetic and multilayer systems, *J. Appl. Phys.* 79 (1996) 6458–6463.
- [35] J. Fidler, T. Schrefl, Micromagnetic modelling of nanocrystalline magnets and structures, *J. Magn. Mag. Mat.* 203 (1999) 28–32.
- [36] F. Reitich, private communication (Dec 1999).
- [37] D. Lewis, J. C. Simo, Conserving algorithms for the dynamics of Hamiltonian systems on Lie groups, *J. Nonlinear Sci.* 4 (3) (1994) 253–299.
- [38] D. Lewis, J. C. Simo, Conserving algorithms for the n dimensional rigid body, *Fields Institute Communications Series* 10 (1996) 121–139.
- [39] H. Munthe-Kaas, Runge-Kutta methods on Lie groups, *BIT* 38 (1998) 92–111.
- [40] A. Iserles, H. Munthe-Kaas, S. Norsett, A. Zanna, Lie-group methods, *Acta Numerica* 9 (2000) 215–365.

- [41] J. C. Simo, L. Vu-Quoc, On the dynamics in space of rods undergoing large motions—a geometrically exact approach, *Comp. Meth. Appl. Mech Eng.* 66 (1988) 125–161.
- [42] J. C. Simo, D. Fox, On a stress resultant geometrically exact shell model. I. Formulation and optimal parametrization, *Comp. Meth. Appl. Mech Eng.* 72 (1989) 267–304.
- [43] D. Lewis, Conserving and approximately conserving algorithms, in: *Dynamics of Algorithms (The proceedings of the IMA Workshop on Dynamics of Algorithms)*, IMA Volumes in Mathematics and its Applications, Vol. 118, Springer–Verlag, New York, 2000.
- [44] D. Lewis, N. Nigam, A geometric integration algorithm with applications to micromagnetics, Tech. Rep. 1721, IMA Preprint Series (August 2000).
- [45] P. Krishnaprasad, X. Tan, Cayley transforms in micromagnetics, *Physica B* 306.
- [46] H. Weyl, *Classical Groups*, Princeton Univ. Press, Princeton, N.J., 1946.
- [47] M. doCarmo, *Differential Geometry of Curves and Surfaces*, Prentice–Hall, Englewood Cliffs, N.J., 1976.
- [48] S. Kobayashi, K. Nomizu, *Foundations of Differential Geometry*, Vol. I, Interscience Publishers, 1963.
- [49] M. Fels, P. Olver, Moving coframes. I. A practical algorithm, *Acta Appl. Math.* 51 (1998) 161–213.
- [50] M. Fels, P. Olver, Moving coframes. II. Regularization and theoretical foundations, *Acta Appl. Math.* 55 (1999) 127–208.
- [51] X.-P. Wang, C. J. García-Cervera, W. E, A Gauss-Seidel projection method for micromagnetics simulations, *J. Comput. Phys.* 171 (1) (2001) 357–372.